



MB-SWIFT functional MRI during deep brain stimulation in rats



Lauri J. Lehto^a, Djaudat Idiyatullin^a, Jinjin Zhang^a, Lynn Utecht^a, Gregor Adriany^a, Michael Garwood^a, Olli Gröhn^{a,b}, Shalom Michaeli^a, Silvia Mangia^{a,*}

^a Center for Magnetic Resonance Research, University of Minnesota, Minneapolis, MN, USA

^b A. I. Virtanen Institute for Molecular Sciences, University of Eastern Finland, Kuopio, Finland

ARTICLE INFO

Keywords:

Multi-band SWIFT
fMRI
Zero-TE fMRI
Blood flow
Deep brain stimulation

ABSTRACT

Recently introduced 3D radial MRI pulse sequence entitled Multi-Band SWEEP Imaging with Fourier Transformation (MB-SWIFT) having virtually zero acquisition delay was used to obtain functional MRI (fMRI) contrast in rat's brain at 9.4 T during deep brain stimulation (DBS). The results demonstrate that MB-SWIFT allows functional images free of susceptibility artifacts, and provides an excellent fMRI activation contrast in the brain. Flip angle dependence of the MB-SWIFT fMRI signal and elimination of the fMRI contrast while using saturation bands, indicate a blood flow origin of the observed fMRI contrast. MB-SWIFT fMRI modality permits activation studies in the close proximity to an implanted lead, which is not possible to achieve with conventionally used gradient echo and spin echo - echo planar imaging fMRI techniques. We conclude that MB-SWIFT fMRI is a powerful imaging modality for investigations of functional responses during DBS.

1. Introduction

Deep brain stimulation (DBS) has successfully treated movement disorders such as Parkinson's disease, dystonia and essential tremor and its use is likely to expand to treating a variety of psychiatric diseases including major depression and obsessive compulsive disorder (Herrington et al., 2016; Holtzheimer and Mayberg, 2011; Johnson et al., 2013). However, the exact mechanisms of neuromodulation induced during DBS treatment still remain unclear (Florence et al., 2016; Herrington et al., 2016). As a tool to detect brain activity during DBS, functional Magnetic Resonance Imaging (fMRI) can inform on the circuitry of the brain function with excellent spatial localization and sufficient temporal resolution.

To date, the feasibility of simultaneous DBS and MRI/fMRI is strongly dependent on the materials used for the DBS leads—commonly constructed of non-ferromagnetic metals (Coffey, 2009)—and potentially hazardous currents in the lead induced by switching of MRI magnetic field gradients and radio frequency (RF) pulses which should be minimized using proper safety protocols (Georgi et al., 2004; Kahan et al., 2015). Thus far, DBS-fMRI studies have been conducted in rats (Lai et al., 2014, 2015; Shih et al., 2014; Van Den Berge et al., 2015; Yang et al., 2013), pigs (Knight et al., 2013; Min et al., 2012; Paek et al., 2015) and humans (Hesselmann et al., 2004; Jech et al., 2001; Kahan et al., 2014;

Phillips et al., 2006; Rezai et al., 1999) using gradient-echo echo planar imaging (GE-EPI). For optimal contrast based on the blood oxygenation level dependent (BOLD) effect (Kim and Ogawa, 2012; Ogawa et al., 1990), the echo time (TE) of the EPI sequence is usually set equal to the transverse relaxation time. With these relatively large TE values and the constrained bandwidth in the phase-encoded dimension, EPI techniques are strongly affected by the large magnetic susceptibility difference between the metallic components of the DBS leads and the tissue. Specifically, the magnetic field inhomogeneities induced by these susceptibility differences cause large image artifacts in the form of geometric distortion and signal dropout that make detecting brain activity near an electrode impossible.

Recently, a 3D radial MRI sequence called SWEEP Imaging with Fourier Transform (SWIFT) (Idiyatullin et al., 2006) was shown to provide functional contrast in the human brain at 4 T, despite the fact that SWIFT has virtually no acquisition delay ($TE \approx 0$) (Mangia et al., 2012). For correct localization of the signal in the presence of large magnetic susceptibility differences, e.g. near the DBS leads, an obvious solution is to utilize SWIFT with very high acquisition bandwidth. Due to its nearly zero acquisition delay, SWIFT can in principle detect all signal surrounding the DBS lead. However, due to technical constraints, the conventional SWIFT sequence has an upper limit on bandwidth (BW). To circumvent that limitation in this work, we thus used a recently

* Corresponding author. University of Minnesota, Radiology Department, Center for Magnetic Resonance Research, 2021 6th St. SE, Minneapolis, MN 55455, USA.

E-mail addresses: lehto041@umn.edu (L.J. Lehto), idiat001@umn.edu (D. Idiyatullin), zhan1029@umn.edu (J. Zhang), [lutecht@umn.edu](mailto:utecht@umn.edu) (L. Utecht), adria001@umn.edu (G. Adriany), gar@cmrr.umn.edu (M. Garwood), olli.grohn@uef.fi (O. Gröhn), micha042@umn.edu (S. Michaeli), mangia@cmrr.umn.edu, mangia@umn.edu (S. Mangia).

introduced version of the SWIFT technique called multi-band SWIFT (MB-SWIFT) (Idiyatullin et al., 2015). MB-SWIFT exploits the sidebands created by gapping the RF pulse and in this manner can achieve high excitation and acquisition BWs. The goal of the present study was to demonstrate the feasibility of MB-SWIFT fMRI during DBS in the rat brain. In addition, the performance of MB-SWIFT in generating functional contrast was compared to that obtained by Spin Echo EPI (SE-EPI), which is grounded on the BOLD effect (Norris, 2012). Finally, we further explored the origin of the fMRI contrast detected with the near zero acquisition delay of MB-SWIFT by changing the flip angle as well as by introducing saturation bands to minimize the effect of blood inflow. The conclusions drawn should be applicable to any other ultra-short-TE MRI technique.

2. Methods

All surgical and experimental procedures were approved by the Institutional Animal Care and Use Committee of the University of Minnesota. Sprague-Dawley rats (Envigo; Madison, WI, USA; n = 10, male, 275–300 g) were initially anesthetized using isoflurane for the duration of the implantation (5% for induction, 2–3% during surgery) in O₂/N₂O 30%/70% carrier gas. The respiration rate was monitored with a plastic pressure sensor during the surgery and MRI scanning. The temperature was maintained at 37 °C with a heating pad during the surgery and with heated water circulation and heated air during MRI scanning. Temperature was monitored with a rectal thermometer. After implanting the electrode, the anesthesia was changed to urethane with three consecutive i.p. injections 15 min apart (1.25–1.50 g/kg) while gradually lowering the isoflurane level, reaching 0% after the last injection. Urethane anesthesia enables a strong BOLD response and it is known to maintain near normal electrophysiology and blood gases in spontaneously breathing animals (Huttunen et al., 2008; Paasonen et al., 2016).

The animal was placed in a stereotactic frame and a 1 mm craniectomy was performed on the right hemisphere. A lead composed of a twisted set of three polyimide-insulated tungsten electrodes (PlasticsOne, MS333T/2C-A/SP; Roanoke, VA, USA) with tip-contact diameters of 200 μm were implanted in the ventral posteromedial nucleus (vpm) (Paxinos and Watson, 1998); ML 2.8 mm, AP –3.4 mm, DV –5.8 mm). 3–4 drops of 2% lidocaine were administered before the incision of the scalp and before cauterizing vessels of the scalp and skull. The remaining hole in the skull around the electrode was filled with gelatin foam (SPONGOSTAN™, Søborg, Denmark). The hole was covered and the electrode was fixed using dental acrylic (Lang Dental, Jet Acrylic, Wheeling, IL, USA). Finally, an Ag/AgCl wire (4 cm long, 0.5 mm diameter) acting as a ground electrode, was inserted below the skin with the tip ending at the base of the neck. When stimulating the vpm, bilateral activation of the somatosensory cortices is expected through the thalamocortical connection between the vpm and cortex (Killackey and Sherman, 2003), and the callosal connection between the cortices (Innocenti, 1986).

All MRI scans were conducted with a 9.4 T 31 cm horizontal-bore magnet equipped with Agilent DirecDRIVE console (Palo Alto, CA, USA) using a quadrature RF coil designed for full rat brain coverage. The coil was composed of materials not visible with ¹H MRI even when using MB-SWIFT, thus ensuring that no unwanted signal would fold into the FOV from the coil itself. Prior to fMRI, anatomical images were acquired using a fast spin-echo (FSE) sequence with exactly the same slice localizations: TR = 3 s, TE_{eff} = 48 ms, number of echoes = 8, matrix size = 256², field of view (FOV) = 3.5² cm², slice thickness = 1 mm and number of slices = 11 with no interslice gaps. The third slice from the posterior was positioned at the center of the electrode. Six rats underwent MB-SWIFT fMRI using the following parameters: TR = 0.97 ms, 3094 spokes per volume, resulting in temporal resolution of 3 s, BW = 192 kHz, matrix size = 64³ and FOV = 3.5 × 3.5 × 6.4 cm³. Separate acquisitions were performed with different flip angles (= 2°, 4° and 6°), while excitation was performed

with a chirp pulse gapped into four 2.6 μs sub-pulses (Idiyatullin et al., 2006, 2015). Two-fold oversampling was used during acquisition in the gaps of 32/BW duration. The post-correlation FID (Idiyatullin et al., 2006) consisted of 32 points. Additionally, as a proof of concept, three animals were imaged with a time resolution of 1 s using 1010 spokes per volume and a flip angle of 6°.

To investigate the contribution of blood flow to the functional contrast, functional scans were also conducted with saturation bands at the back of the brain to saturate the signal of blood inflowing to the brain, or at the front of the brain as a control (n = 5). The saturation bands were repeated after every 32 acquisitions with a rostro-caudal width of 7 mm using a 2 ms sinc pulse with a flip angle of 90°. The centers of the saturation bands were placed at ±8.5 mm rostral/caudal from the center of the electrode. MB-SWIFT parameters were as above, but with 2666 spokes and only flip angle of 6° was used.

The performance of MB-SWIFT was compared to that of SE-EPI (n = 6) with the following parameters: TE = 35 ms, TR = 1.5 s, two shots, resulting in temporal resolution of 3 s, BW = 250 kHz, matrix size = 64², FOV = 3.5² cm², slice thickness = 1 mm and 11 slices with no interslice gaps. The SE-EPI readout direction was set to dorsal-ventral to avoid signal loss in the cortex due to susceptibility differences after exposing the skull. The first three volumes acquired during the stimulation protocol were excluded from the analysis as they consisted of approach to steady state and reference scans for MB-SWIFT and SE-EPI, respectively. The FOV of MB-SWIFT was placed so that the 11 middle slices aligned with SE-EPI and FSE.

The stimulation paradigm consisted of 3 blocks of 60 s of rest and 18 s of stimulation, ending with an additional rest period, resulting in 4 min 54 s of total paradigm. The electrode was driven monopolar using symmetric charge balanced 50 μs square pulses repeated at 20 Hz with amplitude of 0.50–0.75 mA/channel leading to a total current of 1.50–2.25 mA. To avoid adaptation to stimulus, 5 min breaks were taken between trials. The stimulation waveforms were computed and delivered through National Instruments digital-to-analogue converter (cDAQ-9174 chassis, 9263 analogue output module, 9402 digital input/output module; Austin, TX, USA) and three stimulus-isolators (A-M Systems; Carlsborg, WA, USA) using MATLAB 2015b (Mathworks; Natick, MA, USA). The stimulation system was triggered by the scanner with the onset of the pulse sequences through the digital input/output module of the digital-to-analogue converter.

MB-SWIFT images were reconstructed using gridding and iterative FISTA algorithm (Beck and Teboulle, 2009) (3 iterations when using 3 s time resolution and 13 iterations when using 1 s time resolution). The resulting data were analyzed in SPM8 (www.fil.ion.ucl.ac.uk/spm) and MATLAB 2013b. The pre-processing included smoothing with a [2 2 1] pixel FWHM Gaussian kernel, with slice time correction and motion correction for SE-EPI. Because MB-SWIFT is a 3D radial pulse sequence, it is highly insensitive to motion, and thus motion correction was unnecessary. MB-SWIFT with 1 s time resolution was not smoothed. The general linear model consisted of a block design model convolved with a rat hemodynamic function (Silva et al., 2007) and the baseline. Threshold for statistical significance of the activation maps were set to p < 0.05 (family-wise error corrected). Time series analysis was conducted using regions of interest (ROIs) selected with Aedes (aedes.uef.fi). The ROIs included only activated pixels from the ipsilateral and contralateral somatosensory cortex, rostral to the electrode so that the slices with susceptibility artifact using SE-EPI were not included. For the saturation band experiment, ROI drawn on the control scan was used for both data sets. The time series in the ROIs were averaged and corrected for linear trending and baseline. The amplitude of the functional response was estimated as the average of the four highest values during the first stimulation period between 72 and 81 s. Functional signal-to-noise ratios (fSNRs) were estimated by dividing the aforementioned amplitude of the functional response during the first stimulation period with the standard deviation of the baseline prior to the first stimulation period.

3. Results

MB-SWIFT exhibited dramatic improvement in image quality in the presence of an implanted electrode as compared to SE-EPI (Fig. 1). The activation maps obtained with MB-SWIFT and SE-EPI were qualitatively similar, exhibiting ipsilateral and contralateral activations of the somatosensory cortex. The signal loss due to the electrode extended across 2–3 and 5–6 voxels in the medial-lateral direction for MB-SWIFT and SE-EPI (Fig. 1B and C), respectively, and across 2–3 and 4–5 slices in the rostral-caudal direction, respectively, depending on the exact electrode placement within the FOV. The numbers of activated pixels in the somatosensory cortex included in the ROI analysis are compiled in Table 1. The activated area was similar when comparing MB-SWIFT flip angles 4° and 6° to that provided by SE-EPI. Five out of the six animals imaged with flip angles 2°, 4°, and 6° using MB-SWIFT showed activations next to the electrode in the thalamus with flip angle 4° and out of which four animals showed activation with flip angle 6°. Two animals with activations seen with both MB-SWIFT flip angles showed spatially shifted ipsilateral thalamic activations using SE-EPI (e.g. as seen in Fig. 1C). Importantly, MB-SWIFT showed no visible signal pile up artifacts next to the electrode or signal loss near air/tissue interfaces as was observed with SE-EPI.

The time series of the activation in the ipsilateral side exhibited similarity between MB-SWIFT and SE-EPI, although a pronounced flip angle dependence of the activation amplitude was observed with MB-SWIFT (Fig. 2 and Table 1). Ipsilateral fSNR was clearly higher with MB-SWIFT (using flip angle 6°, 27.2 ± 7.8 vs. 11.5 ± 3.1 , $p < 0.05$, Mann-Whitney U test). Contralateral activation also expressed similarity between the pulse sequences, however, flip angle dependence of MB-SWIFT was less evident and no clear difference was observed in fSNR. When comparing the pattern of the responses during the first stimulation period measured with MB-SWIFT and SE-EPI, no statistically significant difference was obtained (point-by-point Mann-Whitney U test, $p_{FDR} > 0.05$ for each point). Finally, in three rats MB-SWIFT data were acquired with a temporal resolution of 1 s, showing excellent spatial agreement with the data obtained using 3 s temporal resolution and no significant deterioration in functional response (Fig. 3). However, these images were clearly more blurred as compared to those acquired with 3 s time resolution.

In order to study the effect of blood flow on the functional response, four animals were scanned with saturation bands placed at different locations of the brain (Fig. 4). When the saturation band was placed in front of the brain, activation was seen in the somatosensory cortex (response amplitude $5.2 \pm 1.7\%$) corresponding to the MB-SWIFT fMRI acquisitions without saturation bands (Figs. 1 and 2). However, when signal of the

blood flowing into the brain was suppressed using saturation bands placed in the back of the brain, the response was significantly reduced ($2.0 \pm 0.8\%$). The number of activated pixels in the ipsilateral cortex for individual animals with saturation band in the back of the brain was 0, 0, 9, 0 and 0 and in the control scans 39, 55, 64, 24 and 74, respectively.

4. Discussion

In this study, we have demonstrated virtually susceptibility artifact free fMRI during DBS in the rat brain using MB-SWIFT. Since MB-SWIFT achieves near zero acquisition delay, nearly all signal surrounding the electrode is preserved regardless of fast T_2^* -decay. Notably, due to the high acquisition bandwidth available with MB-SWIFT, the detected signal is also correctly spatially encoded with no distortion artifacts. The MB-SWIFT functional response showed excellent spatial correspondence with that of SE-EPI. It should be emphasized that the susceptibility artifact free imaging method presented in this work represents a significant advance to aid investigations of functional responses during DBS. Current DBS-fMRI studies are conducted in small and large animal models at clinical scanners (3 T) and at higher magnetic fields have significant limitations due to the impossibility of imaging in the close proximity to an implanted lead, as well as other experimental obstacles such as high sensitivity of EPI to motion and frequently insufficient image quality provided by EPI because of distortions especially at very high fields. The novel near zero acquisition delay modality MB-SWIFT dramatically improves the quality of fMRI data as compared to EPI, and allows fMRI acquisitions in close proximity to an implanted lead with reasonable spatial and temporal resolution. Finally, because MB-SWIFT operates without rapid switching of the gradients, it may be more suitable for fMRI studies from both safety and acoustic noise perspectives. Although most of the currently conducted DBS-fMRI studies are based on the GE-EPI sequence (Georgi et al., 2004; Hesselmann et al., 2004; Jech et al., 2001; Kahan et al., 2014; Knight et al., 2013; Lai et al., 2014, 2015; Min et al., 2012; Paek et al., 2015; Phillips et al., 2006; Rezai et al., 1999; Shih et al., 2014; Van Den Berg et al., 2015; Yang et al., 2013), in this study we chose to use SE-EPI as it can refocus intravoxel dephasing due to the field inhomogeneity caused by an implanted lead. However, any EPI sequence is still sensitive to the field inhomogeneities in the phase encoding direction, as the effective bandwidth is typically in the range of a few kHz. One option for alleviating the susceptibility artifacts is to turn the readout direction perpendicular to the electrode, but still severe artifacts will appear in other locations. As MB-SWIFT is inherently a 3D radial sequence, the acquisition bandwidth is the same in every direction,

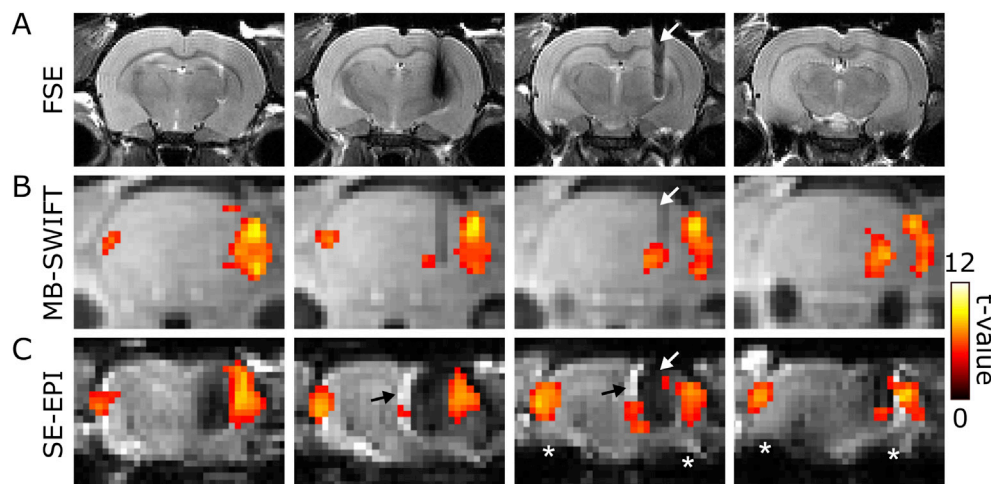


Fig. 1. Functional response of the rat brain to DBS of the ventral posteromedial nucleus at different rostral-caudal slice locations for two different functional acquisition pulse sequences. (A) High-resolution anatomical FSE images of the stimulated region; activation maps in color obtained with (B) MB-SWIFT (flip angle 6°) overlaid on MB-SWIFT images, and (C) SE-EPI, overlaid on a SE-EPI images. The white arrow points on the artifact due to the implanted electrode (A–C); the black arrow and white asterisk in (C) point a signal pile-up artifact near the electrode and magnetic susceptibility artifact due to the tissue/air interface (Li et al., 2015), respectively.

Table 1

Quantification of functional response in the somatosensory cortex as seen by MB-SWIFT and SE-EPI ($n = 6$).

| | # Activated pixels, ipsi | # Activated pixels, contra | Peak response (%), ipsi | Peak response (%), contra | fSNR, ipsi | fSNR, contra |
|-------------|--------------------------|----------------------------|--------------------------|---------------------------|---------------------------|-------------------------|
| MB-SWIFT 2° | 73 ± 26 ^a | 11 ± 10 ^a | 2.2 ± 0.4 ^a | 1.6 ± 0.4 ^a | 14.7 ± 4.4 | 5.4 ± 2.7 |
| MB-SWIFT 4° | 115 ± 31 ^b | 32 ± 19 ^b | 3.6 ± 0.6 ^b | 2.6 ± 0.6 ^b | 22.0 ± 13.1 | 10.5 ± 4.0 ^b |
| MB-SWIFT 6° | 115 ± 27 ^{a,b} | 27 ± 15 ^b | 4.4 ± 0.7 ^{a,b} | 2.6 ± 0.8 ^b | 27.2 ± 7.8 ^{a,b} | 11.9 ± 9.6 ^b |
| SE-EPI | 106 ± 27 | 40 ± 22 | 3.8 ± 0.4 | 3.1 ± 0.3 | 11.5 ± 3.1 | 9.1 ± 3.6 |

p < 0.05, Mann-Whitney U test.

^a Differs from SE-EPI.

^b Differs from flip angle 2°.

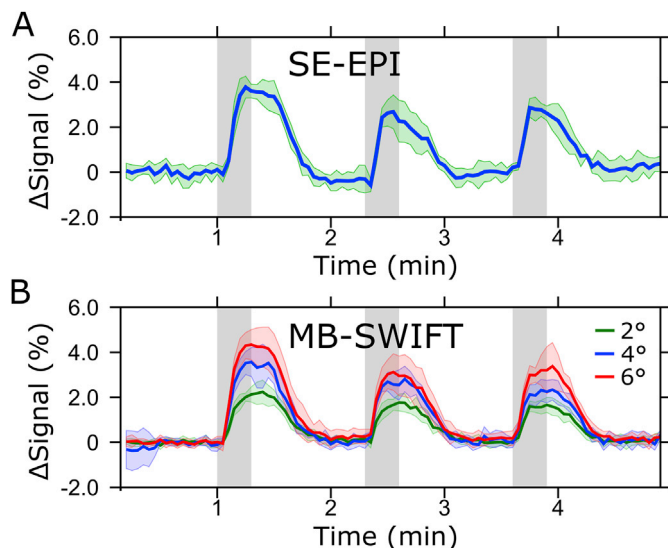


Fig. 2. Mean time series in the ipsilateral ROI drawn in the somatosensory cortex rostral to the electrode artifact ($n = 6$). FMRI response as detected by (A) SE-EPI and (B) MB-SWIFT with different flip angles. MB-SWIFT time courses exhibit significant flip angle dependence. Interanimal standard deviations are indicated by the shaded areas.

allowing the signal to be localized correctly in every direction in 3D space, and even in a close proximity to the electrode's surface. We have demonstrated this in our results in the case of thalamic activation: MB-SWIFT showed thalamic activations immediately adjacent to the electrode, whereas with SE-EPI the activations were spatially shifted and exhibited by fewer animals. The bilateral activation patterns obtained with MB-SWIFT and SE-EPI were similar and consistent with previous studies (Lai et al., 2015; Yang et al., 2013). Further investigation is needed to confirm an exact overlap of activated areas between MB-SWIFT and BOLD. This requires co-registration of the activation maps which was not feasible here due to the severe susceptibility artifacts present in SE-EPI.

Unlike EPI sequences that acquire snapshots in time per slice much faster than the nominal time resolution (or sequence TR for EPI), MB-SWIFT continues to acquire through the whole functional time period. Hence, MB-SWIFT gives a time averaged 3D volume over that time period. Time averaging, or time efficient acquisition, is one reason for the clearly superior ipsilateral fSNR of MB-SWIFT observed in our study. Other factors for the good fSNR are the lack of T_2^* related signal loss, natural oversampling of the center of k-space using 3D radial imaging but likely also more advanced reconstruction (Beck and Teboulle, 2009). In general, the fSNR as a function of flip angle is expected to approximately follow an inverse U-form depending on the inflowing blood's "Ernst angle"—that is related to the circulation time of the blood—and

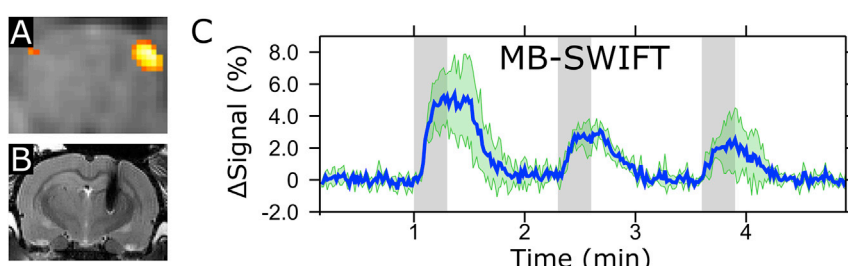


Fig. 3. Functional response using MB-SWIFT using 1 s time resolution and flip angle of 6° ($n = 3$). (A) An activation map overlaid on an MB-SWIFT image, (B) anatomical FSE image of the corresponding slice and (C) mean time series from the ipsilateral somatosensory cortex. Interanimal standard deviations are indicated by the shaded areas in (C).

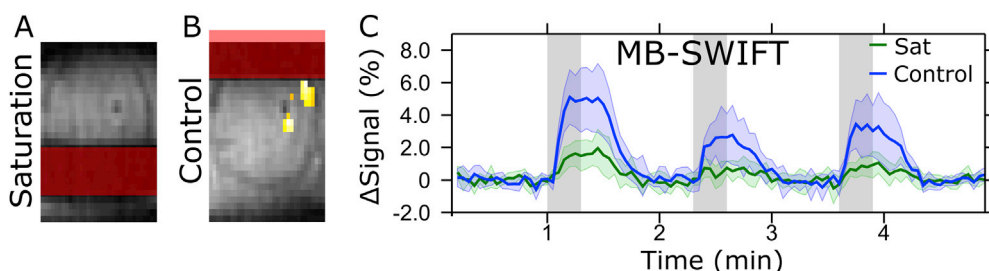


Fig. 4. Functional response using MB-SWIFT with a saturation band. Activation maps ($p_{FWE} < 0.05$) with the saturation band (A) in the back of the brain, (B) in front of the brain and (C) the corresponding mean time series from the ipsilateral somatosensory cortex ($n = 5$, flip angle = 6°). The fMRI contrast is virtually removed by saturating inflowing blood. The red rectangles in (A, B) indicate the placement of the saturation band, and interanimal standard deviations are indicated by the shaded areas in (C).

decreasing SNR of the baseline with increasing flip angle. In this study, we could not achieve higher flip angles than 6° as this required near maximum power output of the RF amplifier.

Our results indicate that the functional contrast detected with MB-SWIFT mainly originates from blood flow increases during activation. The increase in functional contrast detected with larger flip angle of the MB-SWIFT indeed likely reflects the increased T₁ contrast between tissue and increased amounts of T₁-relaxed blood during activation. Additional evidence for the contribution of blood flow is given by the observation that the functional signal was significantly reduced or almost eliminated when utilizing saturation bands that suppressed the contribution of the inflowing blood. Arterial transit time in the sensory cortex—i.e. our region of interest—has been measured as approximately 300 ms when the labeling slice was placed 2 mm caudal of the cerebellum (Thomas et al., 2006). In our experiments, the saturation band covered the cerebellum which likely led to an even shorter arterial transit time. Nevertheless, some T₁ recovery is expected to happen during this shorter transit which may at least partially explain the significantly reduced yet visible functional signal even when applying the saturation band. Thus, since the majority of activation was suppressed in most of the experiments where the saturation band was applied, the main effect contributing to the functional contrast is likely related to blood flow. Flip angle dependence was also shown previously with SWIFT in human using visual stimulation (Mangia et al., 2012). Prior extensive studies of BOLD contrast at high magnetic field 9.4 T suggested that inflow is not a major contributor for GE-EPI, however, increased functional response was shown with decreasing TR and was attributed to perfusion (Wang et al., 2012). Both inflowing blood and perfusion likely contribute to MB-SWIFT since it is not based on T₂* contrast. However, it is possible that the component more directly relevant to neuronal activity, i.e. perfusion, could be extracted from the signal. Currently, MB-SWIFT can be regarded as an alternative, high-CNR method to other T₁ or T₁-weighted mapping efforts to detect brain activation, such as those based on arterial spin labeling techniques (Detre et al., 2012).

Previously, fMRI studies using visual stimulation have also been conducted using 3D ultra-short TE (UTE) at 3 T in humans (Kim et al., 2013). Interestingly, the authors detected only negative responses of approximately -0.5%, while BOLD response was mainly positive at approximately 2.0%. This is opposite to our results and also opposite to previous SWIFT fMRI observations (Mangia et al., 2012). While our first investigations of the origin of the MB-SWIFT functional contrast clearly indicate a predominant role of blood inflow, we cannot rule out that other mechanisms may play a role as well, although likely to a lesser extent.

Zero TE (ZTE) (Hafner, 1994; Madio and Lowe, 1995; Weiger et al., 2011, 2012) could be considered as an alternative to MB-SWIFT. RF pulses used in ZTE consist of a single short hard pulse whereas in MB-SWIFT the pulses are formed of gapped frequency swept chirp pulses with acquisition within the gaps. For both pulse sequences, the excitation profile is described by a *sinc*-function so that acquisition bandwidth is set to the top of the main lobe of the *sinc* (Idiyatullin et al., 2008, 2015). Signal can be excited also outside the acquisition BW by the side lobes though usually, this part of the excitation profile is set outside the RF coil. To maintain a reasonably flat excitation profile within the acquisition BW, pulse length should not exceed 1/2BW (10% drop in excitation profile to the edge of the FOV). Thus, to achieve high BWs with ZTE or MB-SWIFT, very short pulses are required. Hence, when increasing the flip angle for ZTE, peak RF power can be easily reached as only one RF pulse is used inside a TR. In this case, the only way to further increase the flip angle is to increase the pulse length (Weiger et al., 2013) which can compromise the excitation profile. However, since MB-SWIFT uses multiple sub-pulses inside a TR (assumed equal), MB-SWIFT can achieve higher flip angles while maintaining the pulse length and thus relatively flat excitation profile. This advantage will be even more critical for human studies using bigger and less efficient RF coils. It should be noted though that in the version of MB-SWIFT used here, the acquisition time is

directly proportional to the number of sub-pulses and hence ZTE can be more time efficient if hardware restrictions allow this. However, the increased acquisition time of MB-SWIFT could be shortened using super-resolution methods in future work (Idiyatullin et al., 2015). Finally, the excitation profile of MB-SWIFT can be described as “striped”, however, the use of fully frequency swept chirp pulses produce virtually continuous profiles (Idiyatullin et al., 2015).

A crucial aspect of DBS-fMRI is the heating of the leads because of the currents induced by MRI especially with high specific absorption rate (SAR) pulse sequences. Based on the RF power measured at the input of the coil, we estimate that our experiments with MB-SWIFT at 6° flip angle correspond to SAR of ~20 W/kg in the rat head. While this is a large value, by going down to more clinically relevant field strengths, e.g. 3.0 T and 1.5 T, the estimated SAR is reduced to ~2 W/kg and 0.5 W/kg, respectively. According to current manufacturer guidelines for MRI of patients with implanted DBS leads (Medtronic, 2014), the head only SAR limit is 0.1 W/kg at 1.5 T. Hence, further improvements are needed to make MB-SWIFT fMRI more feasible in patients with implanted DBS leads including e.g. reduced flip angle, reduced BW and possibly adding gradient modulation to the acquisition (Zhang et al., 2016). Safety studies of MB-SWIFT in combination with DBS leads are necessary and in general the feasibility of MB-SWIFT fMRI in human should be thoroughly investigated.

As any 3D radial sequence, MB-SWIFT is coil dependent so that all signal detected by the coil needs to be included in the FOV, and as such, this limits the achievable spatial resolution. Given that inflow is the main contributor to the functional contrast of MB-SWIFT, the response is similarly coil dependent. In addition, although true 3D fMRI can be beneficial, its main caveat is the achievable time resolution, as sufficient amount of data needs to be collected in order to avoid aliasing artifacts. Here we demonstrated MB-SWIFT fMRI with 3 s, but also 1 s time resolutions, leading to 76% (3094 spokes) and 92% (1010 spokes) undersampling at the edge of k-space, respectively. Hence, at least moderate time resolutions are achievable with MB-SWIFT and other similar ultra-short-TE MRI sequences. In human scans, the TR from spoke to spoke will likely need to be increased due to the SAR limitations discussed above and due to slower gradient performance. Hence, less data can be acquired per unit of time compared to preclinical scanners. However, as we indeed demonstrated 1 s time resolution with 1000 spokes, time resolutions near 3 s using <3000 spokes resulting in matrix size of 64³ should be feasible for human studies.

5. Conclusion

We have demonstrated that susceptibility artifact free fMRI data can be obtained using MB-SWIFT in the presence of an implanted electrode used for DBS. Our results indicate that the fMRI contrast detected with MB-SWIFT mainly originates from blood flow. The increase in the activation detected with larger flip angle MB-SWIFT is dominated by the increased T₁ contrast between blood and tissue. The contribution of blood flow to the activation was demonstrated by an additional study utilizing saturation bands in the caudal area of the brain which largely suppressed the functional contrast. Our results indicate that with MB-SWIFT fMRI response could be monitored even in the close proximity to an implanted DBS lead. The described strategy may represent an additional step toward intraoperative fMRI during DBS implantation in humans and for future MRI studies of awake animals, due to its immunity to susceptibility and motion artifacts.

Acknowledgements

This work was supported by: the National Institutes of Health (P41 EB015894, P30 NS076408); EU H2020 RISE MICROBRADAM, Professor Pool; WM KECK Foundation; MnDRIVE and The Emil Aaltonen Foundation post-doctoral fellowships to L JL. The authors are grateful to Prof. Kamil Ugurbil for stimulating discussions and comments on the manuscript.

References

- Beck, A., Teboulle, M., 2009. Fast gradient-based algorithms for constrained total variation image denoising and deblurring problems. *IEEE Trans. Image Process.* 18, 2419–2434.
- Coffey, R.J., 2009. Deep brain stimulation devices: a brief technical history and review. *Artif. Organs* 33, 208–220.
- Detre, J.A., Rao, H., Wang, D.J., Chen, Y.F., Wang, Z.J., 2012 May. Applications of arterial spin labeled MRI in the brain. *Magn. Reson. Imaging* 35 (5), 1026–1037.
- Florence, G., Sameshima, K., Fonoff, E.T., Hamani, C., 2016. Deep brain stimulation: more complex than the inhibition of cells and excitation of fibers. *Neuroscientist* 22, 332–345.
- Georgi, J.C., Stippich, C., Tronnier, V.M., Heiland, S., 2004. Active deep brain stimulation during MRI: a feasibility study. *Magn. Reson. Med.* 51, 380–388.
- Hafner, S., 1994. Fast imaging in liquids and solids with the back-projection low angle ShoT (BLAST) technique. *Magn. Reson. Imaging* 12, 1047–1051.
- Herrington, T.M., Cheng, J.J., Eskandar, E.N., 2016. Mechanisms of deep brain stimulation. *J. Neurophysiol.* 115, 19–38.
- Hesselmann, V., Sorger, B., Girnus, R., Lasek, K., Maarouf, M., Wedekind, C., Bunke, J., Schulte, O., Krug, B., Lackner, K., 2004. Intraoperative functional MRI as a new approach to monitor deep brain stimulation in Parkinson's disease. *Eur. Radiol.* 14, 686–690.
- Holtzheimer, P.E., Mayberg, H.S., 2011. Deep brain stimulation for psychiatric disorders. *Annu. Rev. Neurosci.* 34, 289–307.
- Huttunen, J.K., Gröhn, O., Penttonen, M., 2008. Coupling between simultaneously recorded BOLD response and neuronal activity in the rat somatosensory cortex. *Neuroimage* 39, 775–785.
- Idiyatullin, D., Corum, C., Moeller, S., Garwood, M., 2008. Gapped pulses for frequency-swept MRI. *J. Magn. Reson.* 193, 267–273.
- Idiyatullin, D., Corum, C.A., Garwood, M., 2015. Multi-band-SWIFT. *J. Magn. Reson.* 251, 19–25.
- Idiyatullin, D., Corum, C.A., Park, J.Y., Garwood, M., 2006. Fast and quiet MRI using a swept radiofrequency. *J. Magn. Reson.* 181, 342–349.
- Innocenti, G.M., 1986. General Organization of Callosal Connections in the Cerebral Cortex. In: Sensory-motor Areas and Aspects of Cortical Connectivity. Springer, pp. 291–353.
- Jech, R., Urgosik, D., Tintera, J., Nebuzelsky, A., Krasensky, J., Liscak, R., Roth, J., Ruzicka, E., 2001. Functional magnetic resonance imaging during deep brain stimulation: a pilot study in four patients with Parkinson's disease. *Mov. Disord.* 16, 1126–1132.
- Johnson, M.D., Lim, H.H., Netoff, T.I., Connolly, A.T., Johnson, N., Roy, A., Holt, A., Lim, K.O., Carey, J.R., Vitek, J.L., He, B., 2013. Neuromodulation for brain disorders: challenges and opportunities. *IEEE Trans. Biomed. Eng.* 60, 610–624.
- Kahan, J., Papadaki, A., White, M., Mancini, L., Yousry, T., Zrinzo, L., Limousin, P., Hariz, M., Foltyne, T., Thornton, J., 2015. The safety of using body-transmit MRI in patients with implanted deep brain stimulation devices. *PLoS One* 10, e0129077.
- Kahan, J., Urner, M., Moran, R., Flandin, G., Marreiros, A., Mancini, L., White, M., Thornton, J., Yousry, T., Zrinzo, L., Hariz, M., Limousin, P., Friston, K., Foltyne, T., 2014. Resting state functional MRI in Parkinson's disease: the impact of deep brain stimulation on 'effective' connectivity. *Brain* 137, 1130–1144.
- Killackey, H.P., Sherman, S.M., 2003. Corticothalamic projections from the rat primary somatosensory cortex. *J. Neurosci.* 23, 7381–7384.
- Kim, M.J., Jahng, G.H., Lee, S.Y., Ryu, C.W., 2013. Functional magnetic resonance imaging with an ultrashort echo time. *Med. Phys.* 40, 022301.
- Kim, S.G., Ogawa, S., 2012. Biophysical and physiological origins of blood oxygenation level-dependent fMRI signals. *J. Cereb. Blood Flow. Metabol.* 32, 1188–1206.
- Knight, E.J., Min, H.K., Hwang, S.C., Marsh, M.P., Paek, S., Kim, I., Felmlee, J.P., Abulseoud, O.A., Bennet, K.E., Frye, M.A., Lee, K.H., 2013. Nucleus accumbens deep brain stimulation results in insula and prefrontal activation: a large animal fMRI study. *PLoS One* 8, e56640.
- Lai, H.Y., Albaugh, D.L., Kao, Y.C., Younce, J.R., Shih, Y.Y., 2015. Robust deep brain stimulation functional MRI procedures in rats and mice using an MR-compatible tungsten microwire electrode. *Magn. Reson. Med.* 73, 1246–1251.
- Lai, H.Y., Younce, J.R., Albaugh, D.L., Kao, Y.C., Shih, Y.Y., 2014. Functional MRI reveals frequency-dependent responses during deep brain stimulation at the subthalamic nucleus or internal globus pallidus. *Neuroimage* 84, 11–18.
- Li, R., Liu, X., Sidabras, J.W., Paulson, E.S., Jesmanowicz, A., Nencka, A.S., Hudetz, A.G., Hyde, J.S., 2015. Restoring susceptibility induced MRI signal loss in rat brain at 9.4 T: a step towards whole brain functional connectivity imaging. *PLoS One* 10, e0119450.
- Madio, D.P., Lowe, I.J., 1995. Ultra-fast imaging using low flip angles and FIDs. *Magn. Reson. Med.* 34, 525–529.
- Mangia, S., Chamberlain, R., Martino, F., Moeller, S., Corum, C., Kim, T., Kalavagunta, C., Michaeli, S., Garwood, M., Kim, S., 2012. Functional MRI with SWIFT. In: Proceedings International Society of Magnetic Resonance in Medicine.
- Medtronic, 2014. MRI Guidelines for Medtronic Deep Brain Stimulation Systems.
- Min, H.K., Hwang, S.C., Marsh, M.P., Kim, I., Knight, E., Striemer, B., Felmlee, J.P., Welker, K.M., Blaha, C.D., Chang, S.Y., Bennet, K.E., Lee, K.H., 2012. Deep brain stimulation induces BOLD activation in motor and non-motor networks: an fMRI comparison study of STN and EN/GPi DBS in large animals. *Neuroimage* 63, 1408–1420.
- Norris, D.G., 2012. Spin-echo fMRI: the poor relation? *Neuroimage* 62, 1109–1115.
- Ogawa, S., Lee, T.M., Kay, A.R., Tank, D.W., 1990. Brain magnetic resonance imaging with contrast dependent on blood oxygenation. *Proc. Natl. Acad. Sci. U. S. A.* 87, 9868–9872.
- Paasonen, J., Salo, R.A., Shatillo, A., Forsberg, M.M., Narvainen, J., Huttunen, J.K., Grohn, O., 2016. Comparison of seven different anesthesia protocols for nicotine pharmacologic magnetic resonance imaging in rat. *Eur. Neuropsychopharmacol.* 26, 518–531.
- Paeck, S.B., Min, H.K., Kim, I., Knight, E.J., Baek, J.J., Bieber, A.J., Lee, K.H., Chang, S.Y., 2015. Frequency-dependent functional neuromodulatory effects on the motor network by ventral lateral thalamic deep brain stimulation in swine. *Neuroimage* 105, 181–188.
- Paxinos, G., Watson, C., 1998. The Rat Brain Atlas in Stereotaxic Coordinates. Academic Press, San Diego.
- Phillips, M.D., Baker, K.B., Lowe, M.J., Tkach, J.A., Cooper, S.E., Kopell, B.H., Rezai, A.R., 2006. Parkinson disease: pattern of functional MR imaging activation during deep brain stimulation of subthalamic nucleus—Initial experience. *Radiology* 239, 209–216.
- Rezai, A.R., Lozano, A.M., Crawley, A.P., Joy, M.L., Davis, K.D., Kwan, C.L., Dostrovsky, J.O., Tasker, R.R., Mikulis, D.J., 1999. Thalamic stimulation and functional magnetic resonance imaging: localization of cortical and subcortical activation with implanted electrodes. *Technical note. J. Neurosurg.* 90, 583–590.
- Shih, Y.Y., Yash, T.V., Rogers, B., Duong, T.Q., 2014. fMRI of deep brain stimulation at the rat ventral posteromedial thalamus. *Brain Stimul.* 7, 190–193.
- Silva, A.C., Koretsky, A.P., Duy, J.H., 2007. Functional MRI impulse response for BOLD and CBV contrast in rat somatosensory cortex. *Magn. Reson. Med.* 57, 1110–1118.
- Thomas, D.L., Lythgoe, M.F., van der Weerd, L., Ordidge, R.J., Gadian, D.G., 2006. Regional variation of cerebral blood flow and arterial transit time in the normal and hypoperfused rat brain measured using continuous arterial spin labeling MRI. *J. Cerebr. Blood Flow Metabol.* 26, 274–282.
- Van Den Berg, N., Vanhove, C., Descamps, B., Dauwe, I., van Mierlo, P., Vonck, K., Keereman, V., Raedt, R., Boon, P., Van Holen, R., 2015. Functional MRI during hippocampal deep brain stimulation in the healthy rat brain. *PLoS One* 10, e0133245.
- Wang, X., Zhu, X.H., Zhang, Y., Chen, W., 2012. Large enhancement of perfusion contribution on fMRI signal. *J. Cerebr. Blood Flow. Metabol.* 32, 907–918.
- Weiger, M., Brunner, D.O., Dietrich, B.E., Muller, C.F., Pruessmann, K.P., 2013. ZTE imaging in humans. *Magn. Reson. Med.* 70, 328–332.
- Weiger, M., Pruessmann, K.P., Bracher, A.K., Kohler, S., Lehmann, V., Wolfram, U., Hennel, F., Rasche, V., 2012. High-resolution ZTE imaging of human teeth. *NMR Biomed.* 25, 1144–1151.
- Weiger, M., Pruessmann, K.P., Hennel, F., 2011. MRI with zero echo time: hard versus sweep pulse excitation. *Magn. Reson. Med.* 66, 379–389.
- Yang, P.F., Chen, Y.Y., Chen, D.Y., Hu, J.W., Chen, J.H., Yen, C.T., 2013. Comparison of fMRI BOLD response patterns by electrical stimulation of the ventroposterior complex and medial thalamus of the rat. *PLoS One* 8, e66821.
- Zhang, J., Idiyatullin, D., Corum, C.A., Kobayashi, N., Garwood, M., 2016. Gradient-modulated SWIFT. *Magn. Reson. Med.* 75, 537–546.